האוניברסיטה העברית בירושלים
The Hebrew University of Jerusalem

The Faculty of Mathematics and Science,

Edmond Safra (Givat Ram) Campus,

Department of Applied Physics.

Photodetachment of SF_6^- and of small $(SF_6)_n^-$ cluster anions

Thesis submitted for the degree of

"Master of Science"

In Applied Physics

Submitted by Itamar Luzon

ID : 03928017-7

Supervisor: Dr. Daniel Strasser

November 2013

Acknowledgements

This work is dedicated first to my parents, Haim and Tziki Luzon, my sister Shirli Meros and my brothers Tzach and Idan Luzon, for their unconditional love, support and guidance.

It was a great pleasure to work with my supervisor **Dr. Daniel Strasser**, who introduced me to the world of experimental molecular physics and taught me all the experimental techniques. He assisted me throughout my project and without his continuous efforts, this thesis could not have been completed.

I would like to give special thanks to **Dr. Oded Heber**, for spending his valuable time teaching and helping me during the experiments.

To my friends and colleagues Vijayanand Chandrasekaran, Jonathan Toker, Nissan Altstein, Igal Shahar, Uri Lev, Hillel Rubinstein I would like to say thanks for their help and advice.

To my dog Butch who showed her love during the hard times.

I deeply cherish & value the overwhelming understanding and patience, perseverance & encouragement extended by my wife **Noa**.

Abstract

In this work SF_6^- and small $(SF_6)_n^-$ cluster anions are mass selected and trapped in an electrostatic ion beam trap to be interrogated by photodetachment with tunable wavelength ns laser pulses. Photodetachment efficiency curves are constructed by detecting the number of neutral photodetachment products as well as the number of trapped ions as a function of photon energy. With the advent of fast ion beam methods for detection of neutral photo-products and efficient overlap in a co-linear geometry of the laser beam and electrostatically trapped ion beam, we extend the range of SF_6^- photodetachment efficiency measurements towards low photon energies in the range of 420-700nm that are below the detection limit of the previously used method. The shape of the photodetachment efficiency curve is found to be monotonically increasing; in agreement with the curve shape expected based on photoelectron spectroscopy data, indicating no significant contributions of indirect photodetachment processes in the recorded photon energy range. Directly comparing the measured photodetachment efficiency curves for SF_6^- and for small clusters formed by addition of one or two SF_6 molecules, we deduce that the negative charge is localized on one of the SF_6 units within the cluster. We also describe a compact photofragment spectrometer that was designed, constructed and installed inside the electrostatic ion beam trap as a part of this M.Sc. work. In future experiments this new device will allow to pursuit also differential photodissociation measurements in addition to the already described photodetachment efficiency curve measurements.

Table of Contents

1. Background

The work presented here explores the phodetachment of SF_6^- molecular anion and of small $(SF_6)_n^-$ cluster anions. In addition to the basic research interests and applications in accelerator technology, where sulfur hexafluoride is utilized for its high dielectric constant,[1] SF_6 is used in many industrial applications. Its relative inertness and large cross section for electron attachment[2] make SF_6 an efficient electron scavenger used in electrical industry[3], plasma etching processing[4,5] and manufacturing of thin film transistor liquid crystal display.[6] Although SF_6 is an inert gas it is one of the most potent greenhouse gases released to the earth's atmosphere due to its strong IR absorption[7] and its long lifetime in Earth's atmosphere.[8] Interestingly the dominant SF_6 destruction mechanism in the atmosphere is believed to be dissociative electron attachment. Hence its atmospheric lifetime estimates depend strongly on the assumed cross-sections and electron density in the stratosphere, with estimates varying between 10000 years when neglecting dissociative electron attachment and 400 years when assuming each collision event destroys the molecule.[8] As the 100 years global warming potential of SF_6 is 23,900 higher than that of CO_2,[9] SF_6 emissions to the atmosphere are monitored and were shown to grow from ~0.75Gg/yr to ~7.5Gg/yr between 1973 to 2008,[10] compatible with the reported growth of SF_6 sales.[11] Although extensive research efforts were made in the past decade, there is still debate about some of the fundamental properties of the SF_6 molecule.[12] In particular, experimental measurements of the adiabatic electron affinity (EA_{ad}) report values between 0.55-1.20eV.[13–16] While theoretical calculations also result in a wide range of electron affinities 0.73-1.03eV.[12,17] The reported lifetimes of hot metastable SF_6^- anions that are formed by electron attachment vary by many orders of magnitude from 2µs to 1.1sec depending on experimental method.[18–21] Recent storage ring measurements with long storage times showed a non exponential decay of SF_6^- anions with $t^{-1.5}$, extending up to 2sec indicating that the instantaneous decay rate slows down as a function of time.[21] Figure 1. Shows a schematic sketch of the potential curves for the neutral SF_6 and its SF_6^- anion. The addition of an electron significantly changes the equilibrium S-F bond length from 1.56Å to 1.71Å,[22] resulting in a very different vertical electron detachment energy of about 3.1eV,[23] and adiabatic electron affinity(EA_{ad}) of about 1 eV.[12] The large difference leads to a vanishing transition probability from the anion ground state directly to the neutral ground state, consequently resulting in experimental difficulties in EA_{ad} determination. Photoelectron spectroscopy is usually a good method for determining electron binding energies, recent measurements of cold SF_6^- showed unexpected double progression in the photoelectron spectrum[24] that inspired accurate structure calculations. The new calculations indicate that SF_6^- departs from the previously assumed O_h symmetry[22] of SF_6 and has a C_{4v} symmetry, providing an explanation for the observed double progression.[17] The inset of figure 1 shows the suggested SF_6^- structure with C_{4v} symmetry, when the elongated S-F bond length is about 1.9Å and the short S-F bond equilibrium is 1.6Å and the other four S-F bonds are about 1.70Å long. The dissociation energy of SF_6 towards SF_5+F is about ~3.9eV.[25] On the other hand, SF_6^- dissociation energies towards SF_5^-+F and SF_5+F^- are ~1.44eV[12] and 1.75eV respectively,[26] which also lie in the range between the adiabatic detachment and vertical detachment energies. Consequently one can expect SF_6^- to exhibit interesting

competition between detachment and dissociation following absorption of a photon in this energy range. The same competition between detachment and dissociation plays a critical role also in deciding the fate of the SF_6^- formed in electron attachment to SF_6 in the atmosphere. Detachment will return the system back to the neutral molecule, while dissociation will remove SF_6 from the atmosphere.

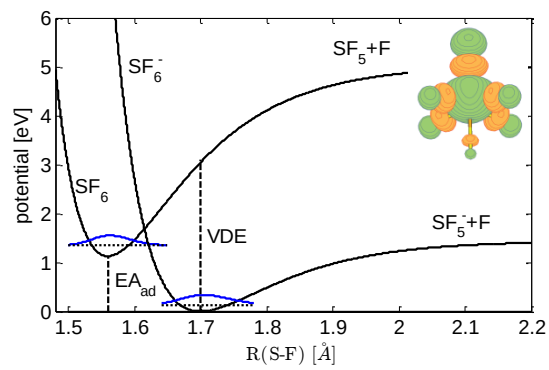

Figure 1: schematic sketch of SF_6 and SF_6^- molecules potential curve (solid black) and their ground state wave functions (solid blue), illustrated by vertical dashed lines the adiabatic and vertical detachment electron energies (EA_{ad}, VDE respectively). in the inset a suggested SF_6^- structure with C_{4v} symmetry.[17]

To help consider the SF_6^- photodetachment, we first explain the photoelectron spectroscopy (PES) measurement performed by Bopp *et al.*[24] and then explain our complementary PDE measurement. In a PES experiment, a photon in the UV is absorbed by the ground state molecular anion and the energy spectrum of emitted photoelectron is recorded. The measured electron kinetic energy can be related, by the energy conservation law, to the energy difference between the anionic ground state and excited neutral molecules:

(1) $$\Delta E = hv - E_k$$

Where ΔE is the difference between the neutral excited state energy and the anion ground state, hv is the photon energy and E_k is the electron kinetic energy.

Figure 2 shows a simplified one dimensional harmonic oscillator model that helps considering the PES process. When equilibrium bond lengths are taken to be 1.56Å and 1.70Å for the neutral and anion respectively, the EA_{ad} is 1eV and the vertical electron detachment energy is 3.1eV. Considering instantaneous photo-detachment from the anionic ground state to the free electron continuum, we can assume the nuclei did not have time to move. Accordingly, the relative probability of producing the different neutral vibrational states can be estimated by the Franck-Condon (FC) aproximation that the transition probability will be proportional to the square of the overlap integral of the initial and final vibrational wave function, also known as the FC factor:

(2) $$FC(v) = \left|\int_{-\infty}^{\infty} \psi_{v(x-x_{neut})}{}^{*} \psi_{0(x-x_{anion})} dx\right|^2$$

Where x_{neut}, x_{anion} are the equilibrium bond lengths, and ψ_v is the vibrational wave function of the *v* state as shown in eq. 3:

$$(3) \qquad \psi_v(x) = \frac{1}{\sqrt{2^v v!}} \left(\frac{m\omega}{\pi\hbar}\right)^{\frac{1}{4}} e^{-\frac{m\omega x^2}{2\hbar}} H_v\left(\sqrt{\frac{m\omega}{\hbar}}x\right)$$

Where v is the vibration number, m is the reduced mass of the nuclei, ω is the angular frequency of the harmonic oscillator and H_v are Hermit polynomials.

The calculated FC factor for the harmonic oscillator model is shown in figure 2 as a function of photon energy. As mentioned before, since the equilibrium bond length is shift by 0.14Å the overlap between the two ground states vanishes. On the other hand, the overlap reaches its maximal value when the energy difference between the final and initial state equals to the potential curve difference at the SF_6^- equilibrium distance. The characteristic vibrational wavefunction illustrated in figure 2 shows the good overlap of the outer lobe of the excited vibrational state and the anion ground state.

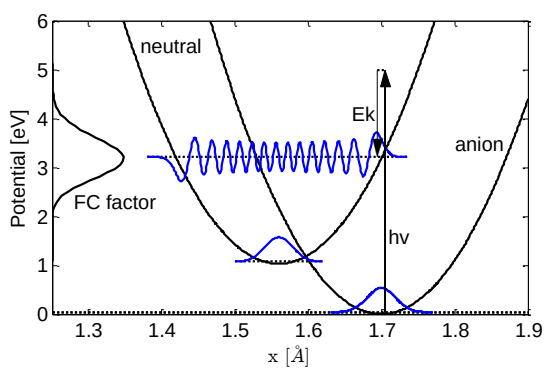

Figure 2: An illustration of photo electron spectroscopy. Scheme of two harmonic oscillator potential, neutral and anion molecule. a photon in the UV (solid arrow) hit the anion, change it to a certain vibration of the neutral molecule by the FC factor (on the left), and the dashed arrow size represent the emitted electron kinetic energy, the end of the dashed arrow is final vibration high and the x-location represent the place in the vibration at the transition.

In the experiments described here we perform a complementary measurement to PES, in which we measure the photo detachment efficiency curve as a function of photon energy (PDE). Figure 3 describes schematically the scenario: a photon is absorbed by the anion, resulting in a superposition of final states including an emission of an electron with different finite kinetic energies and the corresponding energetically allowed final vibrational states of the neutral molecule. As previously described, we can estimate the probability for direct transition to each final state according to the FC principle. Therefore, as illustrated in figure 3, the change in the total detachment probability should be proportional to the sum over all FC factors of the energetically allowed final states, i.e. the states that lie below the energy of the absorbed photon.

$$(4) \qquad PDE \propto \sum_{v=0}^{v_{max}} FC(v)$$

Keeping in mind that the PES spectrum is proportional to the FC factor, one can write the PDE as a function of energy.

(5) $$PDE(h\nu) = \int_0^{h\nu} PES(E)dE$$

When $h\nu$ is the photon energy. However, contrary to PES, PDE can be sensitive also to a possible contribution of indirect detachment mechanisms. i.e. photoabsorption into an excited anion state followed by autoemission as illustrated in equation 6.

(6) $$SF_6^- + h\nu \longrightarrow SF_6 + e^- \ direct$$
$$\hookrightarrow SF_6^{-*} \longrightarrow SF_6 + e^- \ indirect$$

Analysis of electron attachment experiments,[27,28] and theoretical calculations,[29] indicate the existence of such excited SF_6^- states that may in principle contribute to the PDE in the relevant energy range between the vertical and adiabatic detachment energies. As opposed to the monotonously increasing PDE of a direct photodetachment mechanism illustrated in figure 3, indirect contribution can be expected to produce absorption resonances, corresponding to the discrete states of the excited anion.

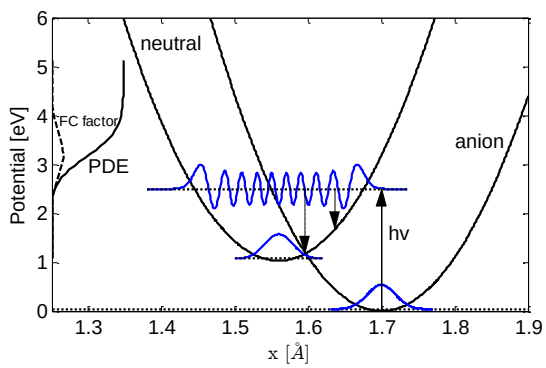

Figure 3: An illustration of photodetachment spectroscopy. approximation of neutral and anion potentials to harmonic oscillator (solid black), the ground states wave function (solid blue), a photon hit the anion molecule (solid arrow), detached an electron and raise to a superposition of all the vibrational levels until the max vibration allows by the photon energy (dashed arrows), and the neutral fragment is measured, on the left side the normalized FC factor (dashed black) and the PDE (solid black) as a function of photon energy.

Figure 4 shows the previously measured PDE of SF_6^- on an absolute cross section scale as function of photon wavelength, reproduced from the work of Mock *et al.*[30] The cross section abruptly vanishes below the experimental detection limit for wavelengths above 400nm corresponding to photon energies below 3.1eV. In my M.Sc. project I extended the SF_6^- PDE measurement beyond the previously available range of 300-400nm to the 420-705 nm wavelengths, corresponding to the 2.94-1.76eV range of photon energies.

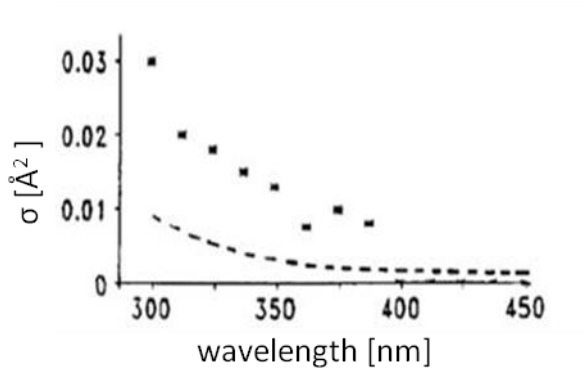

Figure 4: SF_6^- absolute cross section by Mock[30]

Furthermore, harmonic oscillator model calculations shown in figure 5 demonstrate how the PDE in this range is sensitive to even tiny 0.01Å changes in the anion equilibrium bond length, changing both overall magnitude and shape of the PDE curve. I therefore explored also the PDE of small cluster anions based on the SF_6^- system of the $(SF_6)_n^-$ form.[31,32,26] Aiming to determine the effect of the interaction of the SF_6^- anion with the nearby neutral SF_6 molecules on its effective bond length. Although neutral $(SF_6)_n$ clusters are bound by extremely weak Van der Waals, the additional charge changes the induced dipole – induced dipole interactions into a charge – induced dipole interaction. For similarly interacting positively charged rare gas clusters, measurements established that the charge is delocalized over the rare gas cluster, resulting for example in clusters of the form of $Xe_n(Xe_3)^+$ in the case of Xe atoms.[33,34] If such delocalization occurs in $(SF_6)_n^-$ clusters it is bound to modify the effective S-F bond length and strongly affect our PDE curve measurements.

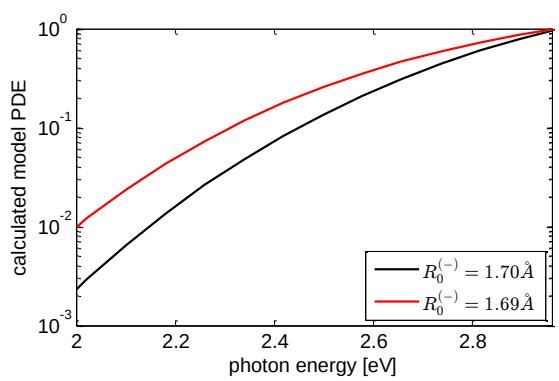

Figure 5: An illustration that come to show the different in the shape for normalized numerical calculation PDE, for a change of 0.01Å in equilibrium bond length, from 1.69Å (red) to 1.70Å (black).

In addition to the PDE measurement setup, I designed and constructed a compact photofragment spectrometer that will enable us to detect and differentiate photo-dissociation products according to their charge over mass ratio and map the competition between detachment and dissociation in this as well as in other molecular anion systems.

2. Experimental setup

Our experimental setup, shown schematically in figure 6, is designed to prepare cold molecular and cluster anions, mass select them and record their photodetachment efficiency as a function of photon energy. Briefly speaking, cold molecular and cluster anions are formed in a pulsed supersonic expansion "Even-Lavie" ion source.[35] The formed ions are then accelerated by 4.2keV and directed towards the Electrostatic Ion Beam Trap (EIBT),[36–39] a resonator composed of two electrostatic mirrors that can trap fast ions oscillating back and forth between the two mirrors. Every experimental cycle, a bunch of ions is injected into the trap by lowering the potential (V_p) on one of the electrodes forming the entrance mirror, thus allowing ions to enter the trap. After the desired ions enter the trap, the potential is raised and effectively traps the ions by closing the "hole" in the mirror. Under UHV conditions (typically10^{-10}_{torr}) the ions oscillate in the EIBT for times as long as 3s and more. As the ion oscillation frequency is proportional to the$\sqrt{\mathrm{q/mass}}$, applying a synchronized periodic ±100 voltage pulse to a deflector (labeled V_{KO}) located inside the trap allows selecting a specific ion species by "kicking out" ions that oscillate at different frequencies.[40] The trapped ions are monitored by observing neutral products of collisions with the residual gas that exit the trap and impinge on an MCP detector located behind the exit mirror. Furthermore, a pickup ring electrode located near the center of the trap allows following the ions directly by observing the image charge induced on the pick-up electrode by the periodic passage of the charged particles.[37,41] A 3mm hole in the center of the MCP detector allows us to efficiently overlap the trapped ion beam with a co-linear laser beam of a pulsed tunable wavelength OPO laser[41]. Neutral products of the laser-anion interaction exit the ion trap and are detected on the MCP outside the trap at a time delay after the laser pulse, corresponding to the velocity of the trapped ions and the product mass. Thus by recording the yield of neutral products and laser power as function of wavelength we are able to construct the photodetachment efficiency curve. Furthermore, as will be explained in section 3.3, applying a high voltage potential on the deflector electrodes in the central region of the trap will allow us to detect also charged photodissociation products and determine their branching fractions by resolving the photo-products by their charge over mass ratio.

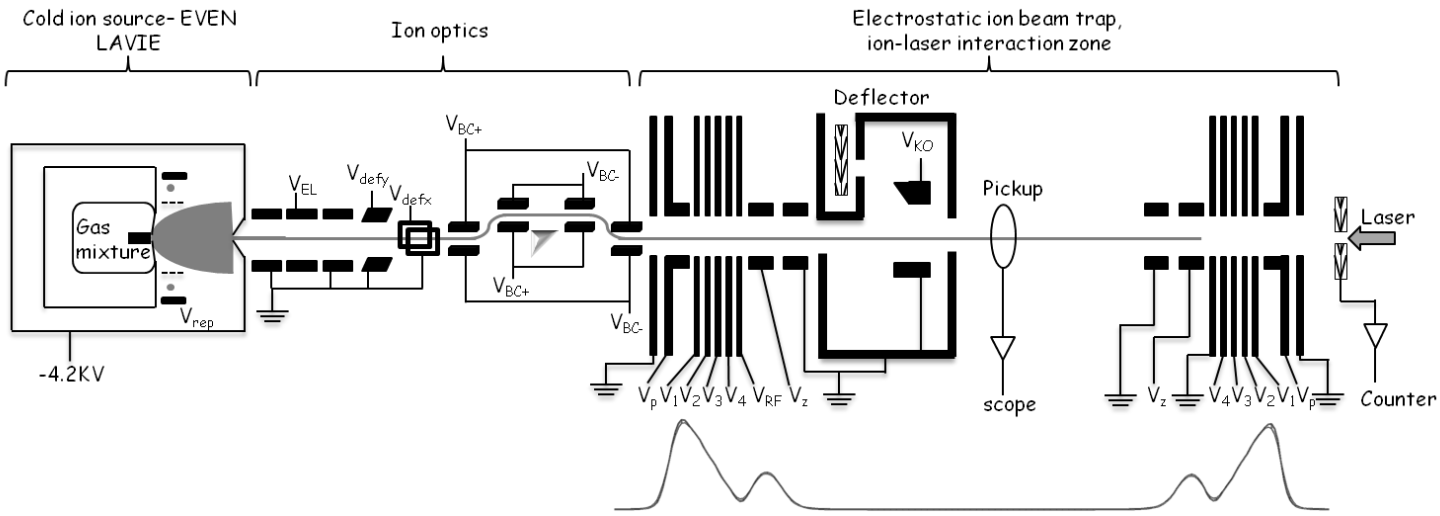

Figure 6: A schematic sketch of the experimental setup, also showing the typical potential along the optical axis of the EIBT. The ion beam induced current measured by Pickup ring, and the neutrals fragments measured by a particles detector in the end of the trap. The curve show the simulated potential that the ion beam feel by the EIBT (V_p,V_1,V_2,V_3,V_4,V_z)

2.1. Ion source and ion optics

SF_6^- and $(SF_6)_n^-$ molecular and cluster anions are generated in a supersonic expansion ion source located on a high voltage platform. The Even-Lavie pulsed valve releases short $8_{\mu s}$ pulses of a specially prepared gas mixture,[35] typically ~420 PSI Neon carrier gas, seeded by ~1% of SF_6 sample gas. The gas pulse supersonically expands into the "source" vacuum chamber that is pumped by a turbo pump to a background pressure of about $5 \cdot 10^{-7}_{Torr}$. A pulsed circular electron gun accelerates 200eV electrons into the expanding gas, generating a variety of cations, anions as well as metastable neutral species. The rapidly expanding carrier gas cools down to temperatures as low as 10K,[35] leading to cooling and even clustering of the sample molecules and ions by multiple collisions with the expanding carrier gas. The supersonic expansion is skimmed by a 3mm skimmer located 100mm downstream of the pulsed valve to select the central coldest part of the expanding gas. After the skimmer, negatively charged species are accelerated by the potential drop from the -4.2kV high voltage platform at the source toward a grounded electrode located at the entrance of ion optics chamber. Thus, the source produces a pulsed beam of anions with a kinetic energy of $q \cdot 4.2Ke$V. As shown in figure 6, the source is followed by ion optics that include an Einzel lens as well as horizontal and vertical deflectors that focus and steer the ion beam into the EIBT with typical voltages of V_{EL}= 2.4KV with V_{defx}=28V, V_{defy}=30V. In addition, four pairs of "beam cleaner" electrodes (V_{BC+}=1.032KV, V_{BC-}=1.038) are pulsed to selectively guide ions arriving at the selected time along a chicane trajectory , while preventing neutral gas molecules as well as ion species with very different charge over mass ratio, which arrive outside the selected time window, from passing to the EIBT. Figure 7 shows a typical single pass pickup signal, recorded while grounding the EIBT electrodes, resolving the charge over mass of the anionic species that we inject into the EIBT based on their time of flight from the ion source to the pickup electrode at the center of the

trap. The most dominant peak belongs to SF_6^-, while the early shoulder is assigned to fragmentation into SF_n^- and the following peaks belong to clusters of the $(SF_6)_n^-$ form.

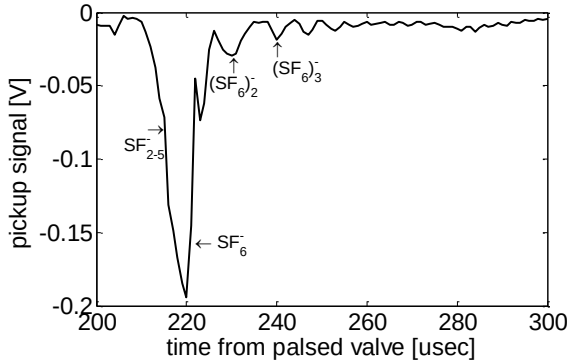

Figure 7: pickup signal measurement of a pulsed ion beam that passing through the pickup. Anions of different $\sqrt{\mathbf{m/q}}$ pass the pickup electrode at different times, producing negative voltage peaks as a function of time. The highest peak (220ms) is a predominantly by SF_6^-, with an unresolved tail towards low TOF composed of SF_n^- with n ranging from 2-5. SF_6^- is followed by $(SF_6)_2^-$ $(SF_6)_3^-$ *et cetera*, arriving respectively at 230ms, 240ms and longer times. The negative voltage indicates negative ions, and the amplitude is proportional to the number of ions.

2.2. Electrostatic ion beam trap (EIBT) , RF and Kick out

The EIBT and its different modes of operation were previously described in detail in a series of manuscripts by Daniel Zajfman *and co-workers*.[36–39] A typical EIBT is made of two electrostatic mirrors and works similar to an optical resonator, supporting stable ion-trajectories that oscillate back and forth between two mirrors. The EIBT is placed in an ultra-high-vacuum chamber, pumped by a cryogenic pump typically to a pressure of 10^{-10}_{Torr} in order to minimize the loss of ions by collisions with the residual gas. Each electrostatic mirror is made of a series of six negative electrodes with radial concentric symmetry that defines a smooth potential. The monotonically rising potential supplied to electrodes 1 - 4 (typically: V_1=-1.622kV, V_2=-3.247kV, V_3=-4.873kV and V_4=-6.5kV) produces a reflecting potential for the 4.2keV ion beam. While the focusing is provided by an Einzel lens, typically supplied with V_z=3.2kV. The additional V_p electrode allows to either open or close the entrance mirror by setting V_p to -1.622kV or -4.42kV respectively. In order to trap a desired species, V_p is lowered to allow ions to enter the trap and is raised back once the desired species passes the pickup. For example: according to the assignments shown in figure 7, SF_6^- ions will be trapped by raising V_p 230µs after the pulsed valve while raising V_p at 245µs will trap $(SF_6)_3^-$ clusters. The ions that are inside the EIBT at the time the mirror is closed are trapped, oscillating between the mirrors. In order to synchronize the motion of specific ion species, a low RF voltage is applied to V_{RF} electrode. We typically use a 4V peak to peak sine wave at the oscillation frequency of the desired species that allows to synchronize the ion bunch to an external trigger and to keep the same ions mass from debunching due to their finite energy spread and trajectory differences.[42] In addition, synchronized square 100V pulses (alternating between positive and negative voltages for

technical reasons) are applied to V_{KO} during the first 100 oscillations, the deflector inside the EIBT, and effectively "kick out" the majority of the ions oscillating out of synch with the desired ion species oscillating at the selected RF frequency[40]. Thus, we obtain a trapped ion bunch mass selected and synchronized to the laser pulse.

2.3. Laser

We are using an EKSPLA tunable wavelength Laser base on optical parametric oscillator (OPO) pumped by a ND-YAG laser.[41] At a repetition rate of 10Hz, the OPO provides ~4ns pulses with tunable wavelength. The OPO signal wavelength is computer controlled in the range of: $420 - 709nm$ with line width of <5cm^{-1} (0.62meV) and scanning step of 0.1nm. The laser beam is further shaped and directed towards the EIBT by a telescope and a set of 3 mirrors that allow passing the laser beam through the 3mm hole in the MCP detector and overlapping it with the optical axis of the EIBT. Figure 8a and 8b show a typical measured output power of the OPO signal and idler as a function of photon energy. Only the OPO signal is used in the experiments described here, due to a combination of vanishing PDE and low laser power below 2 eV photon energies.

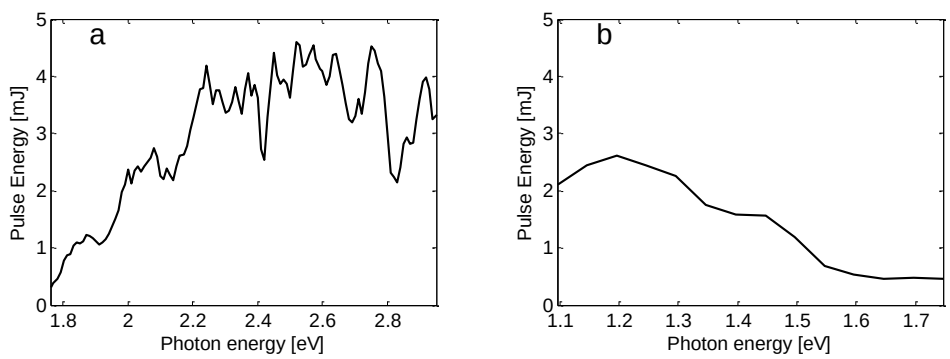

Figure 8 a,b: typical laser pulse energy output from the OPO signal(a) and idler(b).

2.4. Timing and synchronizations

Figures 9a and 9b describe the timing scheme of a typical experiment, showing the sequence of computer controlled triggers supplied to the experimental apparatus. The experiment is synchronized to the laser pulse timing. The first timing signal triggers the pulsed valve, at t=0 which is ~75ms after the previous laser pulse. The delay from the laser pulse is calculated such that the next laser pulses (arriving at 25ms, 125ms and 225ms) will hit the ion bunch when it is at the center of the trap and is moving towards the exit mirror, such that neutral photodetachment products that retain the parent ion velocity move toward the MCP detector. The pulsed valve trigger is followed by a 10μs ionizer pulse, delayed by 69μs. The beam cleaner is typically activated after 208μs for 8μs. As shown in figure 7, SF_6^- anions reach the center of the

EIBT at about 220μs and the EIBT entrance mirror is closed by switching the V_p at 230μs and keeping it high until the end of the cycle at which point remaining ions are released from the trap. Once the trap is closed, a synchronized sine wave is applied to the RF electrode. The periodic "kick out" pulse sequence applied to the V_{KO} deflector electrode for 100 oscillations only and is delayed by a phase of 1.4π with respect to the RF sine wave. The phase shift is optimized for keeping the desired ion bunch, while kicking out all other species with a $\frac{\Delta m}{m} = 7 \cdot 10^{-3}$ mass resolution[40]. It is important to note that it is necessary to match the RF frequency to be an integer times the exact 9.9986Hz repetition frequency of the laser in order to synchronize the ion bunch with more than one laser pulse.

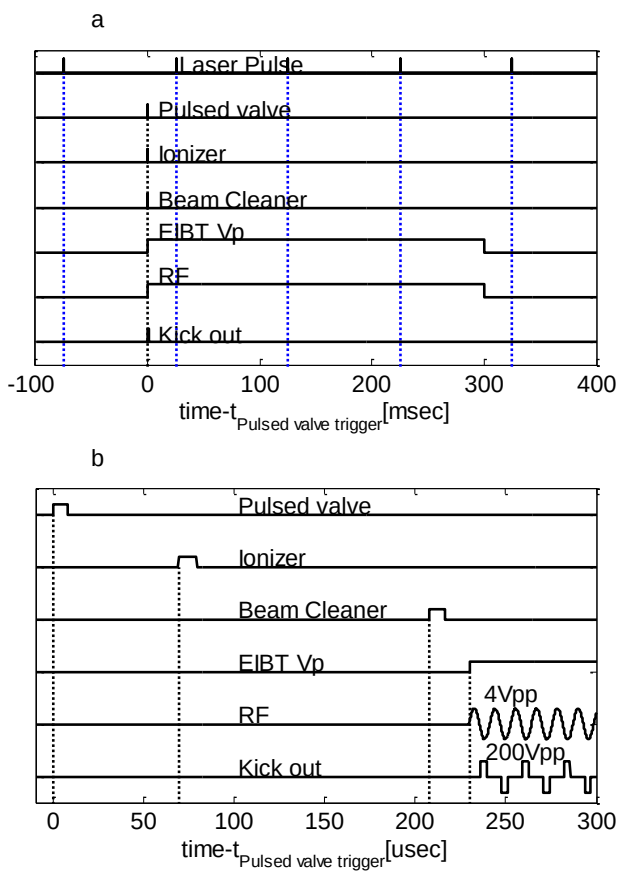

Figure 9 : Experimental timing scheme for SF_6^-: a. show synchronization between the laser to the setup triggers, after the first laser pulse the pulse valve start the sequence, and that the laser hit three times (blue dots) at the trapped ions, while the trapped ions synchronized toward the exit mirror. The Kickout is working for ~1ms, so it's too thin to see its thickness here. b. is a zoom of a to the pulsed valve area to see the different triggers. First a gas realest from the pulsed valve for 8μs, second the gas get ionized for 10μs, third the ion beam get clean from different masses, energies, and neutrals by the Beam Cleaner, and finally trapped inside the EIBT by rising V_p, get into resonant by the RF, and mess selected to the desire ion by the Kickout.

3. Data acquisition

As shown in figure 6, the ions and their neutral products can be detected by three separate detectors: a multi channel plate (MCP)[43,44] that records the impact of neutral products of both ion collisions with the residual gas and neutral products of ion interaction with the laser pulse. The pickup ring electrode that acts as an antenna, measuring the induced image charge of the ion beam inside the EIBT.[38,45] A specially designed compact deflector that I designed, constructed and installed inside the EIBT, which will allow to select product ions according to their charge over mass and detect them on a dedicated micro sphere plate detector (MSP) [46]. The first two detection schemes were previously explained in detail in [38,45], while the compact deflector was designed and built as a part of my M.Sc. work and will be described in more detail here.

3.1. Neutral product detection

Neutral products of the ion beam interaction with residual gas collisions, blackbody radiation[47] and laser pulses are not deflected by the EIBT mirror. Neutrals that fly out of the exit mirror can hit the MCP detector located 67cm after the trap (see figure 6). Although such neutral products have no charge, their high kinetic energy is sufficient to produce a signal on the MCP detector. The small current peaks on the MCP anode are amplified and then discriminated by a constant function discriminator (CFD) producing a digital NIM timing signal, which is converted to a TTL signal and fed into a "NI- PCI-6602 DAQ" PC card that records the neutral products arrival times to the detector with 100ns time resolution, limitted by the maximal counter clock frequency. In order to avoid saturation of the acquisition we limit the maximal count rates to 1 over 100ns by reducing the number of trapped ions and beginning the measurement at 15ms trap time.

3.2. Capacitive pickup ion detection

The time evolution of the ion bunch size and shape is directly and non-destructively measured by a sensitive antenna ring electrode (pickup) that is slightly shifted from the center of the trap towards the exit mirror[42]. The pickup is connected to an amplifier and then recorded on a dedicated scope that records the pickup signal during an entire trapping cycle with sampling frequency of 1MHz. The pickup electrode length is 7 mm and has an inner diameter of 18 mm. The total capacitance of the pick-up electrode, including its support rod and vacuum feed-through is C∼10pF. Due to various slow potential drifts and noises in the lab it is not possible to determine precisely the induced DC charge from the measured voltage. However, the AC image charge induced by the passage of an ion bunch can be determined precisely as will be further explained in the data analysis section 2.2. In order to insure that the ions are all bunched an RF voltage of 4V is applied to the V_{RF} electrode of the trap, effectively bunching the trapped ions[42] allowing us to neglect any DC contribution. We can therefore relate the number of ions in the trap to the area of a pulse produced by the ion bunch as it passes through the pickup. [42]

(7) $$N_{ions} = \frac{C}{L_p}\frac{v}{eq}A$$

Where Lp is the pickup length (7mm), and C in the capacitance (~10pF), v is the ion velocity and A is the area under the oscillation. For example, considering the SF_6^- peak shown in figure 7, A is about 0.1 mV·sec, v is about 70 km/sec, resulting in about $7 \cdot 10^8$ ions in the bunch.

3.3. Ion fragment spectrometer – compact deflector setup

So far the setup allowed detection of the trapped ions and its neutral products, but lack detection of charged ionic products that are blocked by the exit mirror of the trap and cannot reach the MCP detector outside the EIBT. The compact deflector setup is designed to fit inside the EIBT and allow to separate product ions by their kinetic energy. The kinetic energy of a daughter ion can be directly related to its mass by $m_{daughter}/m_{parent} \cdot 4.2$keV, as the kinetic energy released in the dissociation event can be generally neglected compared to the kinetic energy of the beam in the lab frame. With this ability it can resolve daughter ions and measure the branching ratio between the possible charged products. Ion trajectory simulations presented in figure 10 show the trajectory of a trapped ion beam that is deflected with a pulsed voltage applied to the upper deflector electrode (V_{def}) after 200µsec trapping time. The deflection angel depends on the kinetic energy, the charge of the ion and the applied voltage on the upper electrode. In this simulation, a 2150V potential is applied to V_{def}, directing the 4.2 keV ions towards the detector through a narrow 2mm slit . In order to detect daughter ions that have a fraction of the 4.2 keV kinetic energy of the parent ion, a corresponding lower V_{def} is applied.

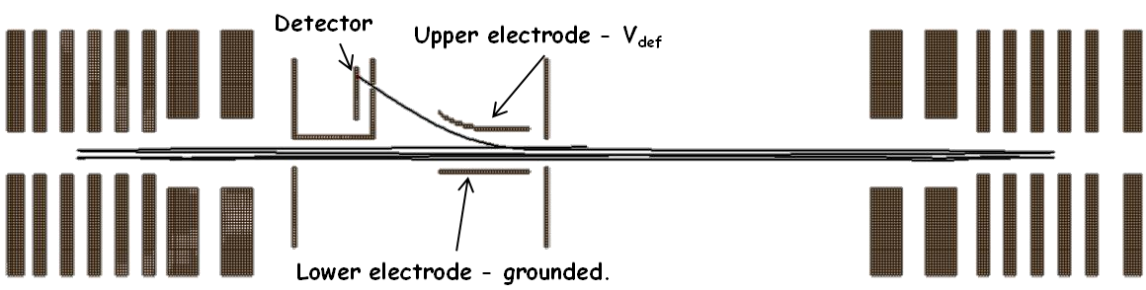

Figure 10: a simion simulation of SF_6^- with kinetic energy of 4.2KeV trapped inside the EIBT for 200µsec, then V_{def} is changed from 0 to 2150V and deflect the ion toward the detector.

Figure 11 shows the simulated correlation between the kinetic energy of ions passing the 2mm slit and the applied V_{def}. Such simulations allowed us to optimize the slit width to obtain the maximal detection efficiency with acceptable daughter ion mass resolution. Figure 12 shows a realistic simulation of detector response as a function of applied potential considering SF_6^- parent ion signal and SF_5^- and SF_4^- daughter ions. The simulation includes an estimated 100eV FWHM Gaussian energy spread of the parent ion beam, a 100meV kinetic energy release in the dissociation process, nevertheless simulation shows that the daughter ions can be clearly mass resolved. Figure 13 shows the mechanical design of the compact deflector setup and its photograph before it was installed in the EIBT system.

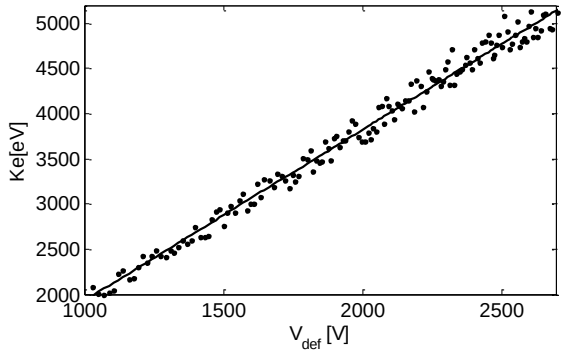

Figure 11: simion simulation that simulated ions that hit the detector, for different energies, with a fit to linear equation result slope of 1.9·Cb.

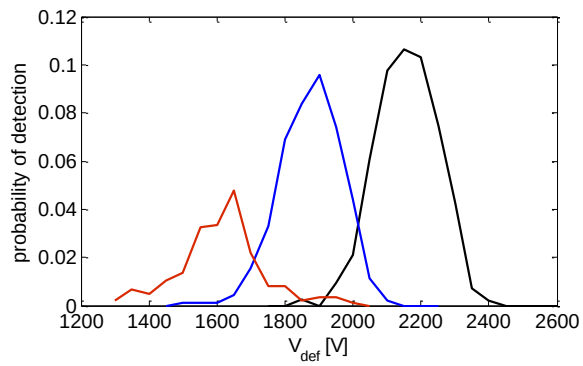

Figure 12: Simulated detection probabilities of SF_6^- (solid black) and its photodissociated daughter fragments of SF_4^- (solid red) and SF_5^- (solid blue) as a function of the upper electrode voltage.

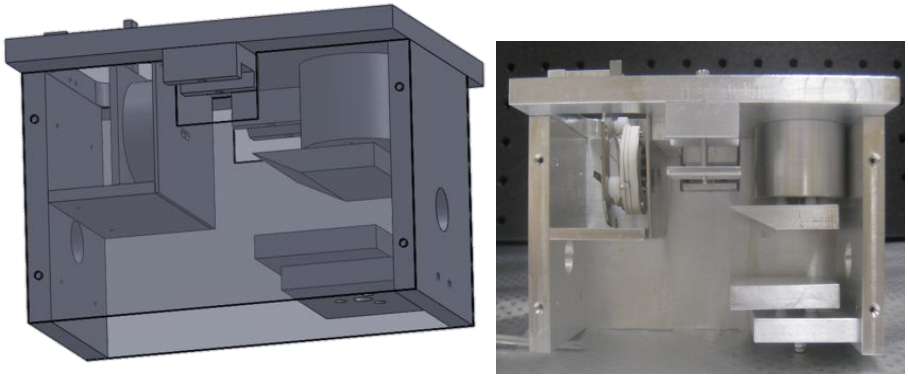

Figure 13 : final design of the deflector (left) and on the deflector before it been installed (right).

4. Data analysis:

In the data analysis section I explain how the raw data collected from the pickup setup and the MCP setup is analyzed to derive the photodetachment efficiency (PDE) curve for a selected ion species as a function of photon energy. In the low flux regime, PDE can be derived according to the following equation:

(8) $$PDE = \frac{1}{F}\frac{N_{product}}{N_{ions}\cdot\Phi}$$

Where $N_{products}$ represents the number of neutral photodetachment products, N_{ions} represents the number of anions and Φ is the photon flux and F is one over the geometric overlap of the ion bunch and the laser beam.

4.1. Measurement of the number of neutral photo-products

Figure 14 shows the MCP signal not in coincidence with a laser pulse, averaged about $2\cdot10^5$ measurements of trapped SF_6^- anions. The signal (N_{mcp}) is predominantly due to neutralization by residual gas collisions and can be related N_{ions} to the number of trapped ions by:

(9) $$N_{mcp}(t) = \eta k N_{ions}(t)dt$$

Where N_{mcp} is the number of hits on the MCP in a dt long time window, η is the detection efficiency of the detector and k is the neutralization rate constant. As will be explained in the following, these average hit rates that are not in coincidence with the laser are subtracted as background to the photodetachment process. As can be clearly seen the decay has more than one component and therefore k is infect a function of time, making it difficult to conclude on the absolute number of trapped ions from a measurement of the neutral yield alone.

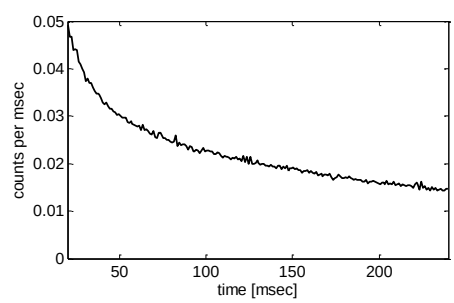

Figure 14 : life time of the neutrals fragments due to residual gas collision detect by MCP

Figure 15 shows a zoomed in view around the time of the laser pulse. The sharp peak at t=0 is due to electronic noise arriving in coincidence with the firing of the laser pulse. For SF_6^- parent ions, neutral photo detachment products born at the center of the trap are expected to arrive in a time window between 8μs and 11.8μs after the laser pulse due to the time of flight (TOF) from EIBT to the MCP. Naturally the time of flight scales with the square root of the parent ion mass for other species, allowing further cleaning of the PDE spectra from possible contaminations of

the ion sample in the data analysis stage. The small tail visible in the log scale representation in figure 15 is due to a negligible number of neutralization events that occur not in the field free region of the trap but in the mirror region that nevertheless arrive to the MCP and produce a measurable signal, albeit arriving with lower speed and at therefore at later times. The periodic background, which is 0.001 times smaller than the photodetachment signal, is due to residual gas collisions and is modulated due to the oscillations of the ion bunch.

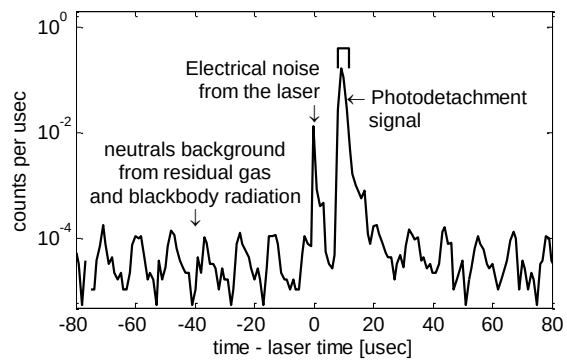

Figure 15: a zoom around the laser time of the raw data average of about $2{\cdot}10^5$ measurements. When after synchronization, the ions-laser photodetachment neutral signal (square marker) comes with the residual gas neutral signal.

Assuming that the decay of the ion beam occurs on long time scales we calculate the average background signal in one oscillation period, $N_{BG}(t)$, using oscillations -26 to -5 and 5 to 26 relative to the laser pulse. The periodic average background is then subtracted from the MCP signal as shown in Figure 16, with a signal to noise level of about $>10^4$.

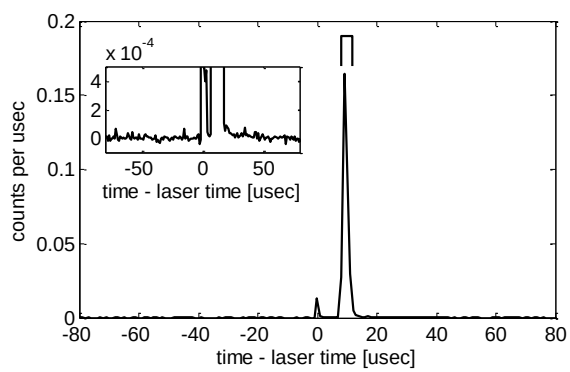

Figure 16: The MCP setup signal around the laser time after a background subtraction, when the photodetachment signal mark with black square, while there is still electrical noise from the laser at zero time. The tale of the signal is neglect to get a better signal to noise ratio.

Since our MCP has a finite size of 40mm diameter with a dead area of 7mm diameter due to the hole in its center, the finite detection efficiency of the detector needs to be evaluated. Following Atia *et al*[48] we rely on a detailed ion trajectory simulation to calculate the acceptance of the

detector. Figure 17 shows the simulated distribution of particle hits on the detector as a function of radial distance. Taking into account the dead area at the center of the MCP we calculate that the geometric acceptance of the detector is 63%. When evaluating the detector efficiency we need also to consider the typical ~58% open area efficiency of the MCP detector[49] to get an overall η ≈ 0.365. We can now evaluate the number of neutral products due to the laser as

(10) $$N_{product} = (N_{MCP} - N_{BG})/\eta$$

Where N_{MCP} and N_{BG} are the total number of counts arriving at the above time window, respectively in and out of coincidence with the laser.

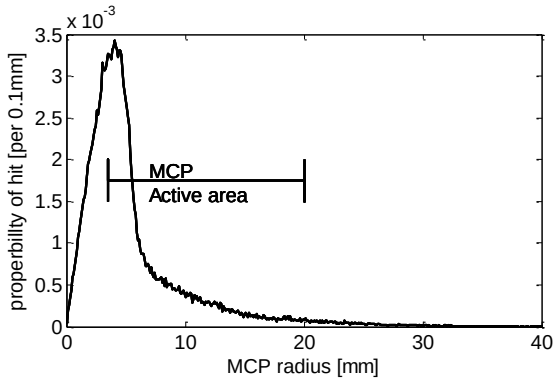

Figure 17: a simion simulation of the active area of the MCP

4.2. Measurement of the number of ions in the trap (N_{ions})

Figure 18a shows a typical raw pickup data averaged over 31 injections, including signal from the SF_6^- ion bunch oscillations as well as a lot of electronic noise. Figure 18a inset shows a zoomed in view of the periodic passes of the ion bunch trough the pick-up electrode. The Fourier transform of the raw data, shown in Figure 18b, clearly shows a strong signal at the frequency of 87062Hz and at its harmonics, corresponding to mass 146amu of SF_6^-.

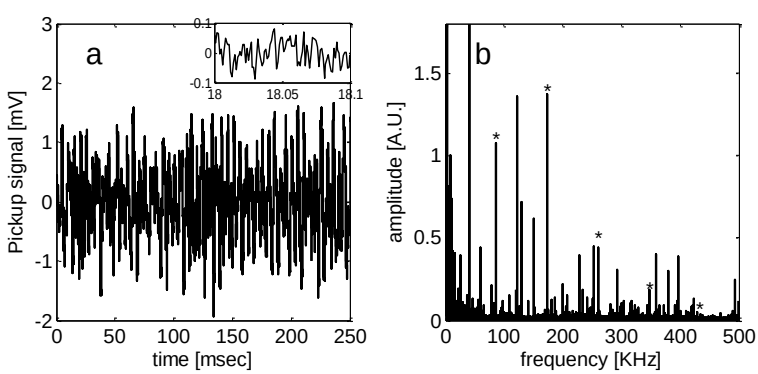

Figure 18: a. raw signal of 31 injections average of the pickup, with phase lock by the RF, when the signal is with a lot of electric noise, the ion beam signal is less then 1mV, in the inset it is able to see a 11.7μs periodic signal. b. show a raw Fourier transform of the signal, it's able to see the ion frequency at 87KHz and its harmonics, as well as a electric noise.

Figure 19a shows the FFT spectrum after application of a filter that passes only the desired frequency and its harmonics. Figure 19a inset shows the Lorentzian shape of the applied filter at the fundamental frequency with a FWHM of 870Hz, selected to preserve bunch dynamics on the few ms and longer time scales that should not affect the sought after time evolution of the number of ions. Intuitively, since the ion bunch pass through the pickup two times each oscillation, one can expect the even harmonics (174KHz, 348KHz) to be stronger than the odd harmonics (87KHz, 261KHz, 435Khz). In fact, following reference[42] we can derive an analytical expression for the harmonics spectrum, assuming Gaussian bunch shapes of width Γ , by performing a Fourier transform on the periodic signal S(t):

$$(11) \qquad S(t) = A(t)\sum_{j=-\infty}^{\infty}\frac{1}{\sqrt{2\pi}\Gamma}\left(\exp\left(-\frac{(t-jT_0)^2}{2\Gamma^2}\right)+\exp\left(-\frac{(t-(j+\kappa)T_0)^2}{2\Gamma^2}\right)\right)$$

Where $A(t)$ is the time dependent area of each temporal peak corresponding to the decaying number of ions, j is the oscillation number and T_0 is the oscillation period. The expressions show two peaks for each oscillation: a forward and a backward pass through the pick-up with κ representing the relative location of the pickup in the trap. In our setup the pick-up is slightly removed from the center of the trap toward the exit mirror, corresponding to κ=0.4511. Equation 12 shows the derived peak intensity of each harmonic.

$$(12) \qquad S_n \propto \sqrt{2+2\cos(2\pi n\kappa)}\cdot\exp\left(-\frac{(n\Gamma/T_0)^2}{2}\right)$$

Where n is the harmonic number, and S_n is the harmonic amplitude. This equation is in agreement with the observed FFT spectrum from figure 18b, where the second harmonic is stronger than first harmonic. Figure 19b shows a zoom on typical filtered pickup signal obtained by inverse Fourier transform. Note that since the image charge is of negative ions, the minima correspond to the ion bunch passing through the pickup and the maxima are when the ion beam is in one of the mirrors. The short and long half oscillations are clearly visible, since the pickup is shifted slightly toward the exit mirror we can assign the times at which the ions are in the field free region moving towards the exit mirror. To capture the evolution of the number of ions as a function of time, we subtract the minima from the maxima signal, averaged over every 200 oscillations and multiply it by $\sqrt{2\pi}\Gamma$ to evaluate the characteristic bunch area as a function of trapping time, $A(t)$. We find that that for our experimental conditions Gamma scales with the oscillation time and was equal to $\Gamma=T_0/12.5$. Using eq. 7 we can now evaluate the number of trapped ions as a function of time. Figure 20 shows the number ions for a typical trapping of SF_6^- , we find that a fit of one exponent can describe good the data, that help us to interpolate the number of ions in the EIBT exactly at the time of laser shot.

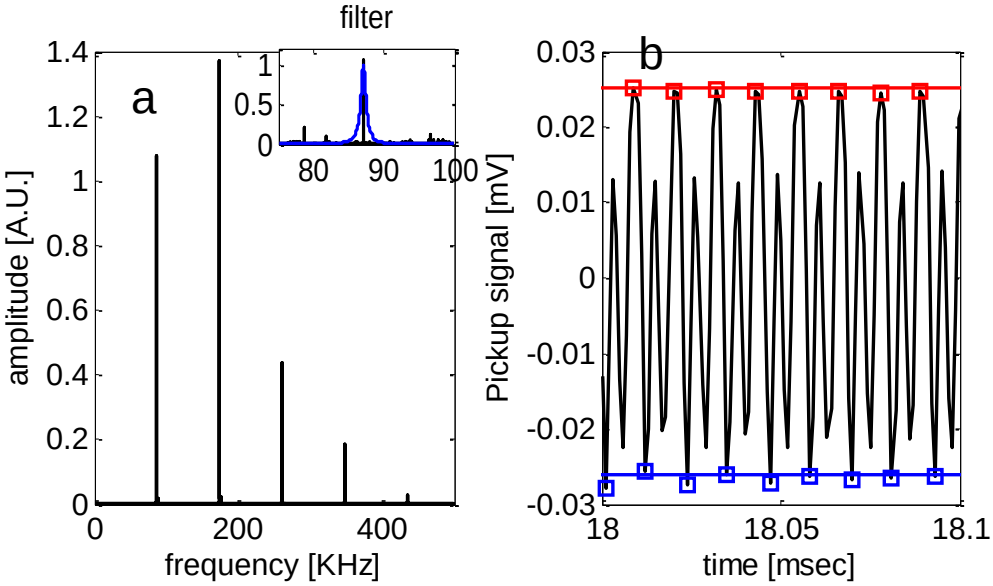

Figure 19 a. a 31 injection average of a clean Fourier signal after Lorentzian filtered, it is able to do that due to the phase lock by the RF. the inset show a zoom on the raw Fourier signal (black line), and the Lorentzian filter (blue line). b. a clean pickup time signal (solid black line), it is easy to see the oscillation of the ion beam. In this figure there is a several element in this figure, 1: The pickup measure the image charge of an anion beam so the min points are the picks of when the ion beam pass inside the pickup and the max point are when the ion beam inside the mirror, 2: The ion beam pass two times through the pickup in each oscillation, therefore there is two picks in every oscillation, a low pick and a high pick, the low pick is when the ion beam is in the entrance mirror side which is farther away from the pickup, the high pick is when the ion beam is in the exit mirror side which is closer, and if the ion beam length is big enough the pickup can also feel some of the ion beam of the next oscillation. Every 200 max and min points of every 1-2 oscillations (red and blue squared respectively) had been chosen to carried out smooth and spline (solid red and blue lines Respectively), the differential between these two lines is proportional the number of ions in the EIBT.

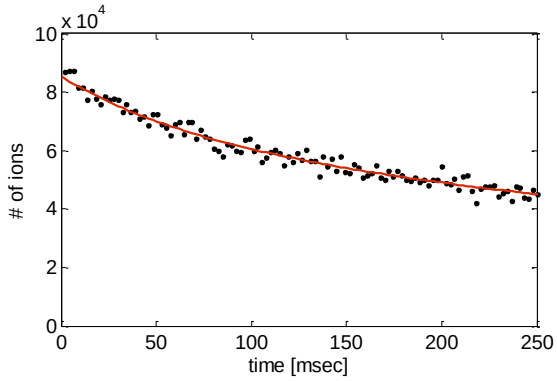

Figure 20: The number of ions in the EIBT calculated by eq. 7 (black dots), with a fit of one exponent (red line) that result the lifetime τ_1=68ms.

4.3. Photo detachment efficiency – PDE

The photon flux Φ is calculate from the measured laser power by dividing the energy per pulse by the photon energy and the evaluated A_{laser}~7.1_{mm^2} area of the laser beam

(13) $$\Phi = \frac{laser\ pulse\ energy}{h\nu \cdot A_{laser}}$$

The same ion trajectory simulation described in the previous section was used to estimate the geometric overlap of the ion bunch (~3mm beam radius) and the laser beam (~1.5mm radius), resulting in a correction factor of F=1/4 described in eq. 8. Combining the number of ions, neutral products and laser flux according to equation 8, figure 21 presents a typical PDE curve of SF_6^-.

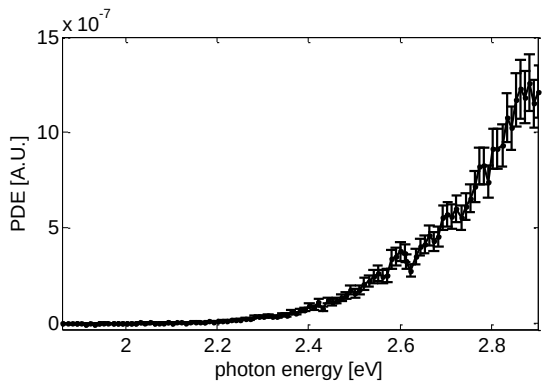

Figure 21: SF_6^- PDE (black dots)

5. Results and discussion

Although ions are formed in a cold ion source, it is still valuable to check for significant changes in the measured PDE curve as a function of trapping time in the room temperature trap environment. Figure 22a shows a comparison of the SF_6^- PDE curve shape for three different laser shots, probing the ions at 25,125 and 225 ms after the ions enter the trap. The three spectra are normalized according to the area under the PDE curve in order to directly compare the shape of the curves. As seen in the figure the structures of the PDE of all three shots look the same within the error bars, which indicates that the PDE of SF_6^- does not change as a function of slow temperature changes during our experiment. In figures 22 a and b we compare the PDE curves recorded at different trapping times for $(SF_6)_2^-$ and $(SF_6)_3^-$ respectively, reaching similar conclusions.

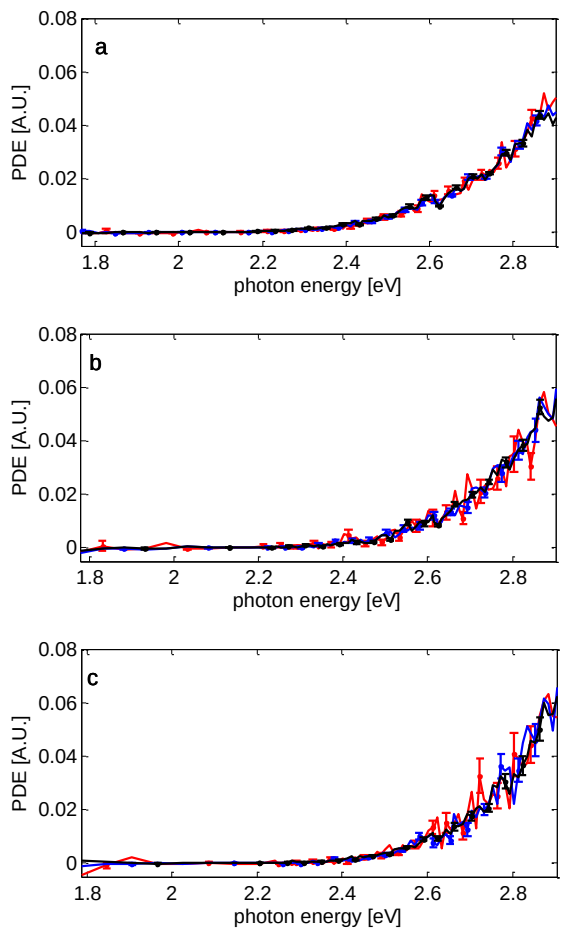

Figure 22 : comparing between the PDEs of SF_6^-, $(SF_6)_2^-$ and $(SF_6)_3^-$ in three different trapping time, 25ms(black), 125ms(blue), 225ms (red) a,b,c respectively.

Combining the data from all three laser shots to obtain better signal to noise ratios we can now compare the PDE curves of SF_6^- to the $(SF_6)_2^-$ and $(SF_6)_3^-$. Figure 23 shows that within the error

bars there is also no big changes in the shape of the PDE curve as one or two neutral SF_6 molecules are added to the SF_6^- anion.

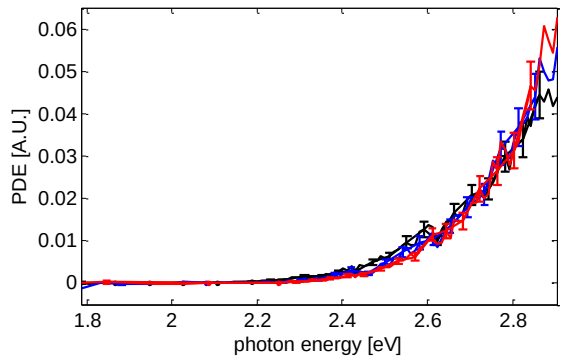

Figure 23: comparing between the PDEs of SF_6^-, $(SF_6)_2^-$ and $(SF_6)_3^-$ (black, blue, red respectively)

To better compare the PDE we use threshold power law function to fit the PDE curve.[50]
To describe the results we use a fit to the function

(14) $$y = a \cdot \theta(E - E_0) \cdot (E - E_0)^n$$

Where θ is a Heaviside function and the free fitting parameters are a scalling factor "a", the power n and the threshold energy E_0l. Figure 24 shows SF_6^- PDE and the fit for the data points of equation 14, for which we obtain fitted power n=4.5±0.8 and thresholds E_0= 1.8±0.1eV, for $(SF_6)_2^-$ and $(SF_6)_3^-$ we obtain similar values. When applying this fit to our harmonic oscillator PDE model calculation shown in fig. 5 and described in the background section, with the anion equilibrium bond length of 1.70Å, EA_{ad}=1eV and including SNR comparable to the experimental conditions, we obtained fitted power n=4.4±0.5 and E_0=1.70±0.1eV. Note that fitted E_0 parameter is not directly indicative of EA_{ad}, even in the modulated PDE.

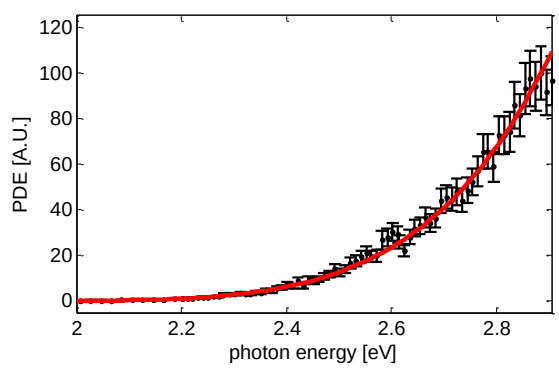

Figure 24: SF_6^- PDE (black) and a fit of equation 14 (red)

Although we expected that adding additional SF_6 molecules to the SF_6^- anion might delocalize the charge and make the anion effective equilibrium bond length smaller, in between the equilibrium bond lengths of SF_6^- anion to SF_6. As was shown in fig 5 that would result in a higher PDE for the low energies tail for the cluster anions compare to SF_6^-. Figure 25 shows the PDE curves of SF_6^- ,$(SF_6)_2^-$ and $(SF_6)_3^-$ and the equation 14 fit to SF_6^- in cyan, we find out that SF_6^-

exhibits a higher tail toward the low photon energies. Figure 26 showing that by calculating the harmonic oscillator PDE model with equilibrium bond length of 1.70Å, EA_{ad}=1eV in zero temperature comparing to room temperature find out that this kind of tail can come from vibrationally hot molecules. Therefore, we assign this small change to relatively hot SF_6^- molecules that can be produced in the low pressure parts of the supersonic expansion due to insufficient cooling. On the other hand, weakly bound dimers and trimers cannot be formed at elevated temperature due to their low binding energies and therefore strictly cold. We conclude that when adding another SF_6 molecules to SF_6^- the charge stayed localized on the SF_6^- anion.

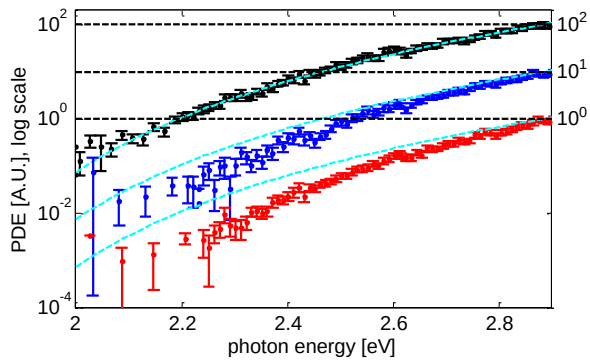

Figure 25: normalized PDE's of SF_6^-, $(SF_6)_2^-$ and $(SF_6)_3^-$ to 1, 10, 100 respectively (black, blue, red respectively), and the fit of equation 14 for SF_6^- (cyan), comparing to each molecule. While the shape of $(SF_6)_2^-$ and $(SF_6)_3^-$ looks similar, SF_6^- have a tail toward the low photon energy, we assume that it come from part of SF_6^- anion created in the source were hot, while $(SF_6)_2^-$ and $(SF_6)_3^-$ are cold.

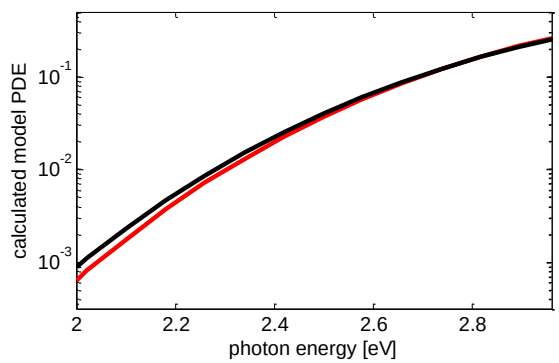

Figure 26: numerical calculated PDE of harmonic oscillator with equilibrium bond length of 1.70Å, EA_{ad}=1eV in zero temperature (red) comparing to room temperature (black)

As we previously explained, when considering only a direct detachment mechanism, the PDE curve should be similar to the sum over the PES spectrum. Figure 27 shows the measured PDE of SF_6^- in our lab compared to an integral over the SF_6^- photoelectron spectrum adopted from Bopp *et al*[24]. We observe that within the error bars there is a very good agreement with no observable indication of contribution from indirect detachment.

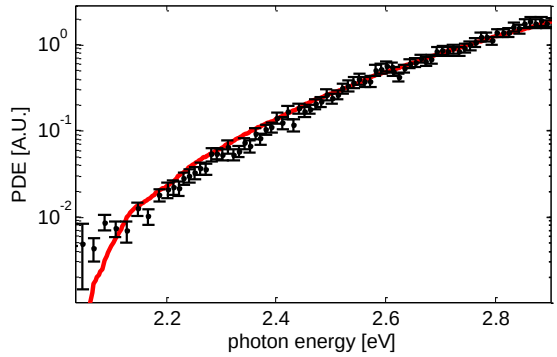

Figure 27: comparing between the SF_6^- PDE (black dots) and the integral on SF_6^- photoelectron spectrum adopted from Bopp *et al*[24] (solid red)

After comparing the shape, using equation 8 we can compare the absolute PDE of different ions. Figure 28 compare between the absolute PDE's of SF_6^- and $(SF_6)_2^-$ (black, red respectively), since within the error bar they have the same PDE, we conclude that the addition SF_6 molecule in $(SF_6)_2^-$ doesn't change the PDE magnitude as well as its shape. On the other hand, when we evaluate the residual gas neutralization rate constant "K", by dividing N_{mcp} by N_{ions} according to equation 9, we get $1.5\cdot10^{-3}$ and $5\cdot10^{-3}$ for SF_6^- and $(SF_6)_2^-$ respectively at t=35ms. This emphasizes the point that photodetachment cross section does not seem to change when adding another SF_6 molecule to the cluster, while collision induced neutralization increase by a factor of 3.33.

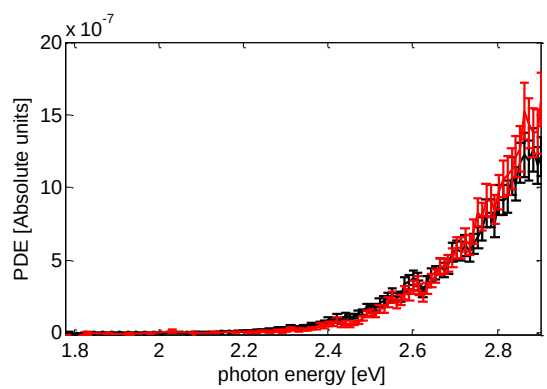

Figure 28: comparing the PDE's of SF_6^- and $(SF_6)_2^-$ (black, red respectively).

Figure 29 Show us absolute photodetachment of SF_6^- adopted from the work of Mock *et al*.[30] Compared to our SF_6^- measurement. Our measurement extended the range of measured photon energies down to 1.8ev, measuring signals that are few orders of magnitude below the detection limit.[30] shown by the dashed line. This was possible due to the use of neutral product detection scheme for efficient fast ion beam technique.

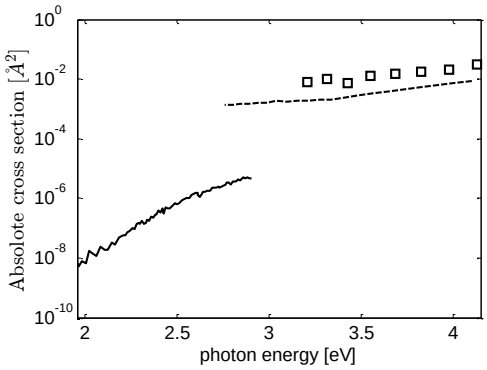

Figure 29: SF_6^- absolute cross section (black squares) and the detection limit (dashed line) from the work of Mock *et al.* [30] completed with SF_6^- PDE measurement.

6. Summery and Conclusions

The photodetachment efficiency curves of SF_6^-, $(SF_6)_2^-$ and $(SF_6)_3^-$ have been measured.

We found that within the error bar all the measurements of the three species have the same shape, except of a small higher tail under 2.3eV for SF_6^- that come from relativity hot ions. We also found that the all the PDE curve shapes are independent of storage time for our experiment time range. We also found the absolute PDE magnitude is the same for SF_6^- and $(SF_6)_2^-$. The good agreement between the integral of privies PES measurement and our PDE curve shape indicate there is no significant contribution from indirect transition as equation 5 suggested. We conclude that the structure of SF_6^-, $(SF_6)_2^-$ and $(SF_6)_3^-$ PDEs are dominated by the SF_6^- anion where the additions SF_6 molecules don't change the PDE. We also design, construct and installed a photo fragment spectrometer that future experiments will use for resolving partial photodissociation cross sections as a function of photon energy.

7. Reference

1. P.G. Ashbaugh,D.W. McAdam, and M. F. J. SF_6 - ITS Properties AND USE as a GASEOUS INSULATOR IN VAN DE GRAAFF ACCELERATORS. *IEEE Trans. Nucl. Sci.* 266 (1965).

2. Newell, W. M. J. and W. R. Absolute elastic differential cross sections for electron scattering from SF_6. *J. Phys. E At. Mol. Opt. Phys.* 24, 473–487 (1991).

3. Qureshi, N. H. Mi. and A. H. A REVIEW OF ELECTRICAL BREAKDOWN IN MIXTURES OF SF_6 AND OTHER GASES. *IEEE Trans. Electr. Insul* EI-14, 1 (1979).

4. Hussain, S. Q. *et al.* Light trapping scheme of ICP-RIE glass texturing by SF6/Ar plasma for high haze ratio. *Vacuum* 94, 87–91 (2013).

5. Gharooni, M. *et al.* A novel non-sequential hydrogen-pulsed deep reactive ion etching of silicon. *J. Micromechanics Microengineering* 23, 095014 (2013).

6. Cheng, J.-H., Bartos, S. C., Lee, W. M., Li, S.-N. & Lu, J. (Ching-H. SF_6 usage and emission trends in the TFT-LCD industry. *Int. J. Greenh. Gas Control* 17, 106–110 (2013).

7. Ko, M. K. W. *et al.* Atmospheric Sulfur Hexafluoride ' Sources , Sinks and Greenhouse Warming. 98, (1993).

8. Reddmann, T., Ruhnke, R. & Kouker, W. Three-dimensional model simulations of SF_6 with mesospheric chemistry. *J. Geophys. Res.* 106, 14525 (2001).

9. Houghton, et al. GWPs and atmospheric lifetimes of halocarbons and other halogenated compounds. *IPCC SAR* (1996). at <http://www.ipcc.ch/ipccreports/sres/emission/index.php?idp=123>

10. Rigby, M. *et al.* History of atmospheric SF_6 from 1973 to 2008. *Atmos. Chem. Phys.* 10, 10305–10320 (2010).

11. Brenninkmeijer, C. A. M. Atmospheric SF_6 : Trends , Sources , and Prospects. *Environ. Sci. Technol* 32, 3077–3086 (1998).

12. Troe, J., Miller, T. M. & Viggiano, A. A. Communication : Revised electron affinity of SF_6 from kinetic data Communication : Revised electron affinity of SF_6 from kinetic data. *1. Troe J, Mill. TM, Viggiano AA. Commun. Revis. electron Affin. SF6 from Kinet. data Commun. Revis. electron Affin. SF_6 from Kinet. data. 2012;1211021–4.* 136, 121102 (2012).

13. Compton, R. N., Reinhardt, P. W. & Cooper, C. D. Collisional ionization between fast alkali atoms and selected hexafluoride molecules. *J. Chem. Phys.* 68, 2023 (1978).

14. Streit, G. E. Negative ion chemistry and the electron affinity of SF_6. *J. Chem. Phys.* 77, 826 (1982).

15. Chen, E. C. M., Wiley, J. R., Batten, C. F. & Wentworth, W. E. Determination of the electron affinities of molecules using negative ion mass spectrometry. *J. Phys. Chem.* 98, 88–94 (1994).

16. Viggiano, A. A., Miller, T. M., Friedman, J. F. & Troe, J. Low-energy electron attachment to SF6 . III . From thermal detachment to the electron affinity of SF_6. *J. Chem. Phys.* 127, 244305 (2007).

17. Eisfeld, W. Highly accurate determination of the electron affinity of SF_6 and analysis of structure and photodetachment spectrum of SF_6^-. *J. Chem. Phys.* 134, 054303 (2011).

18. Gerchikov, L. G. & Gribakin, G. F. Electron attachment to SF_6 and lifetimes of SF_6^- negative ions. *Phys. Rev. A* 77, 042724 (2008).

19. Appelhans, A. D. & Delmore, J. E. Refinement of the autoneutralization lifetimes of short lived states of SF−6. *J. Chem. Phys.* 88, 5561 (1988).

20. Liu, Y., Suess, L. & Dunning, F. B. Rydberg electron transfer to SF_6 : Product ion lifetimes. *J. Chem. Phys.* 122, 214313 (2005).

21. Rajput, J., Lammich, L. & Andersen, L. H. Measured Lifetime of SF_6^-. *Phys. Rev. Lett.* 100, 153001 (2008).

22. Borrelli, R. Franck – Condon analysis of the SF_6^- electron photodetachment spectrum. *Chem. Phys. Lett.* 445, 84–88 (2007).

23. Gutsev, G. & Bartlett, R. Adiabatic electron affinities of PF5 and SF_6: a coupled-cluster study. (1997).

24. Bopp, J. C. *et al.* Spectroscopic Characterization of the Isolated SF_6^- and $C_4F_8^-$ Anions : Observation of Very Long Harmonic Progressions in Symmetric Deformation Modes upon Photodetachment. *J. Phys. Chem. A* 111, 1214–1221 (2007).

25. McMillen, D. F. & Golden, D. M. Hydrocarbon Bond Dissociation Energies. *Annu. Rev. Phys. Chem.* 33, 493–532 (1982).

26. Wang, Y., Champion, R. L., Doverspike, L. D., Olthoff, J. K. & Van Brunt, R. J. Collisional electron detachment and decomposition cross sections for SF_6^-, SF_5^-, and F^- on SF_6 and rare gas targets. *J. Chem. Phys.* 91, (1989).

27. Fehsenfeld, F. C. Electron Attachment to SF6. *J. Chem. Phys.* 53, (1970).

28. Avrillier, S. & Schermann, J.-P. Vibrational excitation of SF_6 by electron impact. *Opt. Commun.* 19, 87–91 (1976).

29. Gutsev, G. L. THE STRUCTURE OF THE SF 6 MOLECULE AND THE SF_6^- ANION EXCITED STATES G. L. Gutsev. *Inst. Chem. Physics, Russ. Acad. Sci.* 5622, 504–510 (1992).

30. Mock, R. S. & Grimsrud, E. P. Electron photodetachment of the molecular anions of SF_6 and several perfluorinated hydrocarbons. *Chem. Phys. Lett.* 184, 99–101 (1991).

31. Ingólfsson, O. & Wodtke, A. Bridging the Cluster-to-Bulk Divide: Electron Attachment Time-of-Flight Mass Spectrometry Reveals Geometrical Shell Closings in $(SF_6)_n$ Clusters (n=2 – 550). *Phys. Rev. Lett.* 87, 183401 (2001).

32. Ingolfsson, O. & Wodtke, A. M. Electron attachment time-of-flight mass spectrometry reveals geometrical shell closings in van der Waals aggregates. *J. Chem. Phys.* 117, 3721 (2002).

33. Haberland, H. *et al.* Electronic and Geometric Structure of Ar_n^+ and Xe_n^+ Clusters: The Solvation of Rare-Gas Ions by Their Parent Atoms. *Phys. Rev. Lett.* 67, 3290–3293 (1991).

34. Gascón, J. a., Hall, R. W., Ludewigt, C. & Haberland, H. Structure of Xe_n^+ clusters (N=3–30): Simulation and experiment. *J. Chem. Phys.* 117, 8391 (2002).

35. Even, U., Jortner, J., Noy, D., Lavie, N. & Cossart-Magos, C. Cooling of large molecules below 1K and He clusters formation. *J. Chem. Phys.* 112, 8068 (2000).

36. Zajfman, D. *et al.* Electrostatic bottle for long-time storage of fast ion beams. *Phys. Rev. A* 55, R1577–R1580 (1997).

37. Strasser, D. *et al.* Negative Mass Instability for Interacting Particles in a 1D Box: Theory and Application. *Phys. Rev. Lett.* 89, 283204 (2002).

38. Pedersen, H. *et al.* Diffusion and synchronization in an ion-trap resonator. *Phys. Rev. A* 65, 042704 (2002).

39. Andersen, L. H., Heber, O. & Zajfman, D. Physics with electrostatic rings and traps. *J. Phys. B At. Mol. Opt. Phys.* 37, R57–R88 (2004).

40. Toker, Y. *et al.* The kick-out mass selection technique for ions stored in an Electrostatic Ion Beam Trap. *J. Instrum.* 4, P09001–P09001 (2009).

41. Wu, S., Blake, G. a, Sun, Z. & Ling, J. Simple, high-performance type II b-BaB2O4 optical parametric oscillator. *Appl. Opt.* 36, 5898–901 (1997).

42. Rahinov, I., Toker, Y., Heber, O., Strasser, D. & Rappaport, M. Lifetime measurements in an electrostatic ion beam trap using image charge monitoring. *Rev. Sci. Instrum.* 83, 033302 (2012).

43. WIZA, J. L. Microchannel plate detectors. *Nucl. INSTRUMENTS METHODS* 162, 587–601 (1979).

44. Matsuura, S., Umebayashi, S., Okuyama, C. & Oba, K. Characteristics of the Newly Developed MCP and Its Assembly. *IEEE Trans. Nucl. Sci.* 32, 350–354 (1985).

45. Heber, O. *et al.* Electrostatic ion beam trap for electron collision studies. *Rev. Sci. Instrum.* 76, 013104 (2005).

46. Naaman, R. & Vager, Z. An electron multiplier capable of working at low vacuum: The microsphere plate. *Rev. Sci. Instrum.* 67, 3332 (1996).

47. Toker, Y. *et al.* Blackbody-induced radiative dissociation of cationic SF6 clusters. *Phys. Rev. A* 86, 023202 (2012).

48. Attia, D., Strasser, D., Heber, O., Rappaport, M. L. & Zajfman, D. Transverse kinematics of ions stored in an electrostatic ion beam trap. *Nucl. Instruments Methods Phys. Res. Sect. A Accel. Spectrometers, Detect. Assoc. Equip.* 547, 279–286 (2005).

49. Straub, H. C., Mangan, M. a., Lindsay, B. G., Smith, K. a. & Stebbings, R. F. Absolute detection efficiency of a microchannel plate detector for kilo-electron volt energy ions. *Rev. Sci. Instrum.* 70, 4238 (1999).

50. Strasser, D. *et al.* Tunable wavelength soft photoionization of ionic liquid vapors. *J. Phys. Chem. A* 114, 879–83 (2010).

מבוא

בעבודה זו האניון SF_6^- וצברים קטנים של אניוני $(SF_6)_n^-$ נבררים על ידי מסה ונכלאים במלכודת יונים אלקטרוסטטית על מנת להחקר עם לייזר ננו-שניות באורך גל משתנה. עקומות יעילות לתלישת אלקטרון נבנו על ידי מדידת פוטו-תוצרים נייטרלים ומדידת מספר היונים הכלואים כפונקציה של אורך גל. מאז שהופיעו השיטות של מדידת פוטו-תוצרים נייטרלים של קרן יונים מהירה עם קרן לייזר קוליניארית בחפיפה טובה וכליאת יונים אלקטרוסטטית, הרחבנו את הטווח עקומות יעילות לתלישת אלקטרון לטווח של 420-700ננומטר שנמצא מתחת לגבול המדידה של השיטה הקודמת שנוסתה. הצורה של עקומת יעילות לתלישת אלקטרון של SF_6^- נראית מונוטונית עולה בהתאמה עם המידע שהתקבל ממדידת העקומה הספקטרוסיקופית הפוטו-אלקטרונית, דבר המצביע על כך שלא התבצע מעבר עקיף במהלך תלישת האלקטרון בטווח האורכי גל שנמדד. השוואה ישירה של עקומות היעילות לתלישת אלקטרון עבור האניון SF_6^- וצבירים קטנים של אניוני $(SF_6)_n^-$ שנוצרים על ידי הוספה של אחד או שני מולקולות של SF_6, מוצאת שהאלקטרון ממקום על אחד ממולקולות הSF_6 שבצביר. אנחנו גם מתארים ספקטרומטר של פוטו-תוצרים אניונים, שתוכנן, נבנה והותקן בתוך המלכודת יונים האלקטרוסטטית כחלק מעבודת המוסמך שלי. בעתיד רכיב זה יוכל למדוד את יחס התוצרים האניונים השונים שנוצרים בתהליך בליעת הפוטון בנוסף למדידת עקומות יעילות פוטו-ניטרלית.

האוניברסיטה העברית בירושלים
The Hebrew University of Jerusalem

הפקולטה למתמטיקה ולמדעי הטבע,

קמפוס אדמונד דה ספרא (גבעת רם),

המחלקה לפיסיקה יישומית

חתך פעולה לתלישת אלקטרון של SF_6^- ושל צבירי אניוני $(SF_6)_n^-$ קטנים

עבודת מחקר לשם קבלת תואר מוסמך

בפיסיקה יישומית

איתמר לוזון

ת.ז. 03928017-7

מנחה: ד"ר דניאל סטראסר

נובמבר 2013